THE AMERICAN SOCIETY OF MECHANICAL ENGINEERS
345 E. 47 St., New York, N.Y. 10017

92-G

Experimental and Computational Investigation of the NASA Low-Speed Centrifugal Compressor Flow Field

M. D. HATHAWAY
U. S. Army Combat and Material Research Labs
Cleveland, Ohio 44135

R. M. CHRISS, J. R. WOOD and A. J. STRAZISAR
NASA Lewis Research Center
Cleveland, Ohio 44135

ABSTRACT

An experimental and computational investigation of the NASA Low-Speed Centrifugal Compressor (LSCC) flow field has been conducted using laser anemometry and Dawes' 3D viscous code. The experimental configuration consists of a backswept impeller followed by a vaneless diffuser. Measurements of the three—dimensional velocity field were acquired at several measurement planes through the compressor. The measurements describe both the throughflow and secondary velocity field along each measurement plane. In several cases the measurements provide details of the flow within the blade boundary layers. Insight into the complex flow physics within centrifugal compressors is provided by the computational analysis, and assessment of the CFD predictions is provided by comparison with the measurements. Five-hole probe and hot-wire surveys at the inlet and exit to the rotor as well as surface flow visualization along the impeller blade surfaces provide independent confirmation of the laser measurement technique.

NOMENCLATURE

$\hat{c}$	Unit vector in the measured velocity component direction
J	Streamwise measurement grid indice
$\vec{g}$	Local streamwise grid direction vector
$\hat{g}_m$	Unit vector in local meridional grid direction
$\hat{g}_p$	Unit vector in local pitchwise grid direction
$\hat{g}_s$	Unit vector in local spanwise grid direction
m/m_s	Non-dimensional shroud meridional distance
N_{cpp}	Number of encoder counts per blade pitch
N_p	Number of impeller blade passages
PS	Pressure surface
r/r_t	Radius non-dimensionalized by exit tip radius
SS	Suction surface
U_t	Impeller tip speed, m/sec
$\vec{V}$	Absolute total velocity vector, m/sec
V_c	Mean velocity component measured in direction $\hat{c}$, m/sec
V_m	Meridional velocity component, m/sec
V_p	Pitchwise secondary velocity component, m/sec
V_{qm}	Quasi-meridional velocity component, m/sec
V_r	Radial velocity component, m/sec
V_s	Spanwise secondary velocity component, positive towards the shroud, m/sec
V_{st}	Velocity component tangent to the shroud meridional direction, m/sec
V_T	Total relative velocity, m/sec
V_z	Axial velocity component, m/sec
V_θ	Relative tangential velocity component, m/sec
α	Flow pitch angle, deg., $\alpha = tan^{-1}(V_r/V_z)$
β	Absolute flow angle, deg., $\beta = tan^{-1}(V_\theta/V_{qm})$
θ	Tangential coordinate, radians

Superscripts

$\bar{}$	Passage average

INTRODUCTION

The complex curvature of centrifugal compressor impeller blade channels, coupled with strong rotational forces and clearance between the rotating impeller and stationary shroud generate secondary flows in unshrouded impellers which transport low momentum fluid into the main stream of the impeller passage. The ability to reduce the resultant flow non-uniformities at the impeller exit by altering new impeller designs to control the secondary flow development may therefore lead to improved performance. In order to succeed, such a design activity must be guided by an improved understanding of the flow physics within the impeller and by reliable numerical flow field predictions.

Several previous investigators have provided flow field measurements within unshrouded centrifugal compressor impellers. Eckardt's laser anemometer measurements in a radial-outflow im-

Presented at the International Gas Turbine and Aeroengine Congress and Exposition
Cologne, Germany June 1-4, 1992
This paper has been accepted for publication in the Transactions of the ASME
Discussion of it will be accepted at ASME Headquarters until September 30, 1992

peller provided the first experimental evidence in high-speed impellers of the development of a "wake" of low momentum fluid near the suction surface/shroud corner of the blade passage (Eckardt, 1976). Krain (1988), Krain and Hoffman (1990), Ahmed and Elder (1990), Sipos (1991), and Rohne and Banzhof (1991) have acquired laser anemometer measurements in backswept impellers which indicate that the wake develops near the shroud at mid-pitch.

Due to the small passage size and optical access limitations in these previous investigations, few experimental details of the secondary flow development inside high—speed impeller passages are available. Krain (1988) and Sipos (1991) have therefore used vortex models to infer the vortical nature of the secondary flow from the flow angle measurements which they were able to acquire on blade-to-blade streamsurfaces.

Several low-speed investigations have also provided some insight into secondary flows. Senoo, *et al.*, (1968) used dye in a water-flow experiment to visualize the tip clearance flow. Farge, *et al.*, (1989) performed 5–hole pressure measurements in a 1 meter diameter shrouded impeller which rotated at 500 rpm. A clearance gap was left between the blade tip and the impeller shroud in order to generate a tip clearance flow. However, as the authors point out, there is no relative motion between the blade and the shroud, so the physics of the tip clearance flow in this investigation is not the same as it would be in an unshrouded impeller. Fagan and Fleeter (1991) used laser anemometry to measure all three velocity components in a low speed, shrouded, mixed-flow compressor.

In lieu of detailed experimental measurements of the secondary flow fields in unshrouded impellers, several investigators have recently shown secondary flow details generated using three—dimensional Navier-Stokes numerical simulations (Krain and Hoffman, 1989, 1990; Hah and Krain, 1990; Bansod and Rhie, 1990; Moore and Moore, 1990). Fagan and Fleeter (1991) have also shown calculated secondary flow field results for their shrouded impeller.

The purpose of the present investigation is to provide a detailed experimental study of primary and secondary flow development within an unshrouded centrifugal compressor impeller. A Low Speed Centrifugal Compressor (LSCC) which has an exit diameter of 1.52 meters has been specifically designed and commissioned to meet this objective. The LSCC was designed to generate a flow field which is aerodynamically similar to that found in high-speed subsonic centrifugal compressors. The large size of the impeller enables the measurement of all three velocity components throughout the impeller blade passage.

Laser anemometer measurements and surface flow visualization results are presented and compared to a prediction of the flow field generated using Dawes' three-dimensional Navier-Stokes code (Dawes, 1988). The processes which lead to the formation of the throughflow momentum wake which is characteristic of unshrouded centrifugal compressor impellers are clearly explained using results from both the CFD and experimental effort. The results indicate that low momentum fluid near the blade surfaces migrates outward toward the tip of the blade and becomes entrained into the tip clearance jet. In addition, low momentum fluid near the blade tip is transported to the pressure side/shroud corner of the blade passage where it accumulates to form the wake.

Measurements acquired downstream of the impeller are also presented to illustrate how the flow field non-uniformities which exist at the impeller exit mix out through the vaneless diffuser. Finally, the flow field measurements obtained in the LSCC are compared to those measured a high-speed impellers by Krain and Hoffman (1989, 1990) to assess the degree to which the flow physics in the LSCC simulates the flow physics within a high-speed centrifugal impeller.

TEST COMPRESSOR

The NASA Low-Speed Centrifugal Compressor (LSCC) is an experimental facility designed to duplicate the essential flow physics of high-speed subsonic centrifugal compressor flow fields in a large low-speed machine in which very detailed investigations of the flow field can be made. A complete description of the facility is provided by Wood, *et al.*, (1983) and Hathaway, *et al.*, (1991).

The test compressor is a backswept impeller with a design tip speed of 153 m/sec. The impeller is followed by a vaneless diffuser in order to generate an axisymmetric outflow boundary condition which is desirable for CFD analysis of an isolated blade row. The impeller has 20 full blades with a backsweep of 55 degrees. The inlet diameter is 0.870 m and the inlet blade height is 0.218 m. The exit diameter is 1.524 m and the exit blade height is 0.141 m. The tip clearance between the impeller blade and the shroud is 2.54 mm, and is constant from the impeller inlet to the impeller exit. This tip clearance is 1.8% of the blade height at the exit of the impeller. The blade surfaces are composed of straight-line elements from hub to tip. This feature enabled fabrication of the impeller by a flank-milling process on a 5-axis milling machine. This feature also facilitates acquisition of laser anemometer measurement of velocities close to the blade surfaces by enabling the laser anemometer optical axis to be directed parallel to the blade surface.

The research operating point selected for both computational and experimental investigations of the LSCC flow field was set at standard–day corrected conditions of 30 kg/sec and 1862 rpm, which is near peak efficiency, for all data presented herein.

INSTRUMENTATION AND MEASUREMENT TECHNIQUE

Separate laser windows provide optical access to the impeller in each of three regions: the impeller inlet, knee and exit. Each window has compound curvature and matches the shroud contour in both the streamwise and circumferential direction in order to maintain the proper impeller tip clearance throughout the compressor. A meridional view of the LSCC, see Figure 1, shows the spanwise and streamwise locations at which laser anemometer data have been acquired. The cross-channel measurement stations which are numbered denote the stations at which data will be presented. The station numbers are the streamwise indices of a body-fitted measurement grid which was used to position the laser measurement point within the impeller. The measurement grid used in this investigation divides the streamwise blade length into a series of "quasi-orthogonal", or near-normal, cross-channel planes. Stations 23, 85, 118, 135, 165, and 170 are located at -40, 14, 47, 64, 94, and 99 percent of meridional shroud length. The four measurement stations in the vaneless diffuser (172, 173, 175, and 178) are at impeller tip radius ratios of 1.01, 1.02, 1.04, and 1.06.

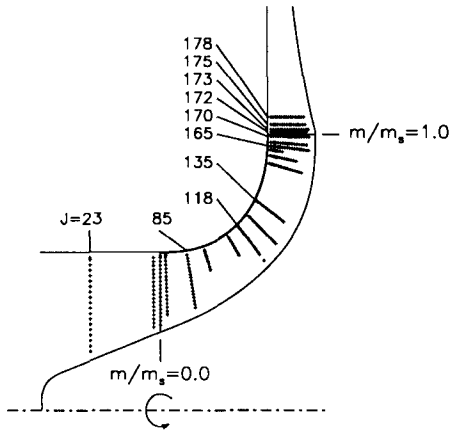

Figure 1 Meridional View of LSCC rotor showing laser anemometer measurement locations.

Laser Anemometer and Data Acquisition

A two-component laser fringe anemometer operating in on-axis backscatter mode was used in this investigation. Frequency shifting was used for both fringe systems to provide directional sensitivity for all velocity measurements.

Two digital shaft angle encoders (one for each laser anemometer channel) were used to generate a fixed number of pulses for each rotor revolution. When a laser velocity measurement occurred, the current encoder count was recorded along with the velocity data. The encoder count indicates the circumferential location of the velocity measurement relative to a once-per-rev timing mark on the impeller. In the present investigation, the encoders were set to generate N_{cpp}=200 counts per pitch across each of the 20 impeller blade channels. Further details of the encoding technique are described by Strazisar, *et al.*, (1989) and Wood, *et al.*, (1990).

The velocity component measurements acquired at each encoder count are first arithmetically averaged to determine the mean of each measured velocity component, V_c, where subscript c denotes that the velocity was measured in the direction of the unit vector $\hat{c}$. The mean velocities are then averaged across the 20 blade channels as shown in Equation 1, to yield a single "passage-averaged" velocity profile for each velocity component which is representative of the profile across each individual blade passage:

$$\overline{V_c}(i) = \frac{1}{N_p}\sum_{j=1}^{N_p} V_c(i + N_{cpp} * j),\ i = 1, N_{cpp} \qquad (1)$$

The normalized difference

$$\frac{\overline{V_c}(i) - V_c(i + N_{cpp} * j)}{\overline{V_c}(i)} \qquad (2)$$

where $\overline{V_c}(i)$ is the passage-averaged velocity component at any pitchwise location i and $V_c(i + N_{cpp} * j)$ is the mean velocity component in blade passage j at the same pitchwise location, has been checked and the difference is generally less than 1%. This indicates that the passage-averaging process does not appreciably alter any of the blade-to-blade velocity profile details. All of the data presented in this report are based on passage-averaged velocity distributions.

In most regions of the flow field, 50,000 velocity measurements were acquired at each (axial, radial) measurement point shown in Figure 1. This would yield an average of 250 measurements at each of the 200 points in the passage-averaged velocity distribution if the measurements were evenly distributed across the blade pitch. However, in general the number of measurements were not evenly distributed across the pitch. Therefore, the total number of measurements had to be adjusted in order to maintain a reasonable number of measurements in regions across the pitch where the data rate was low.

Seeding Technique

Polystyrene latex (PSL) spheres, manufactured using the process developed by Nichols (1987), were used as the seed material. Due to limitations in the manufacturing tolerance, the mean size of the seed particles produced for a given batch of seed varied from batch to batch, although the standard deviation of the particle sizes for a given batch of seed was generally less than 0.01–0.03 μm. The mean size of the seed particles used during the course of this investigation varied from 0.8 μm to 0.95 μm.

The seed material manufactured by Nichols' technique consists of a dilute suspension of PSL spheres in water. This mixture is further diluted in pure ethyl alcohol. The seed/water/alcohol mixture is injected into the airstream approximately 3 meters upstream of the impeller leading edge using air-driven atomizing nozzles. The alcohol and water quickly evaporate, leaving individual PSL particles suspended in the airstream.

Extensive in-situ particle size measurements were made with an aerodynamic particle sizer prior to making laser anemometer measurements to insure that the seeding scheme was operating properly. The sizer was used to analyze samples of the airstream which were extracted through a pitot tube located at measurement station 23 ahead of the impeller. No particles could be detected ahead of the impeller when pure alcohol was injected through the spray nozzles. The sizer was also used to analyze air samples when seed particles were added to the alcohol carrier to insure that individual seed particles did not agglomerate into groups of larger particles.

Three-Dimensional Velocity Measurement Technique

In order to determine all three components of the total velocity vector at a point in the flow field, two velocity components are measured at each of two different orientations of the laser anemometer optical axis. The two orientations of the optical axis were selected to minimize the amount of the blade passage which is optically blocked by the blade while maintaining a 20–30 degree included angle between the two orientations in order to minimize propagation of uncertainty of the measured velocity components into the calculated components. The resultant four measured components are combined using a least squares fit (Equation 3) to yield the total three-dimensional velocity vector,

$$\frac{\partial\left[\sum_{k=1}^{4}\left(\vec{V}\cdot\hat{c}_k - \left(\overline{V_c}\right)_k\right)^2\right]}{\partial\vec{V}} = 0 \qquad (3)$$

where $\hat{c}_k$ is the unit vector in the k^{th} measurement direction, $\vec{V}$ is the absolute total velocity vector which is to be determined, and $(\overline{V}_c)_k$ is the measured passage-averaged velocity component in the direction of $\hat{c}_k$. As a check, the projection of the calculated total vector in the direction of each of the four measured components is compared to the measured component. The difference is generally less than 2% of the measured component.

The emphasis in the measurement technique described above was in obtaining the spanwise velocity component since this component has not been measured by most previous laser anemometer investigations in centrifugal compressors and is by far the most difficult component to resolve in most turbomachinery applications. The ability to measure the spanwise velocity component was verified upstream of the impeller at station 23 (shown in Figure 1) by comparing the pitch angle, α, derived from the laser anemometer measurements to the pitch angle measured by a 5-hole probe. The results of this exercise, shown in Figure 2, indicate that the laser measurement technique is capable of accurately measuring the relatively small pitch angles which exist near the shroud. The agreement between the laser and 5-hole probe measurements of the pitch angle is better than 2 degrees over the outer 70% of span (0.20 m immersion). The laser measurements tend to depart from the 5-hole probe measurements at lower spans, which is probably due to the effect of window curvature which distorts the laser measurement volume.

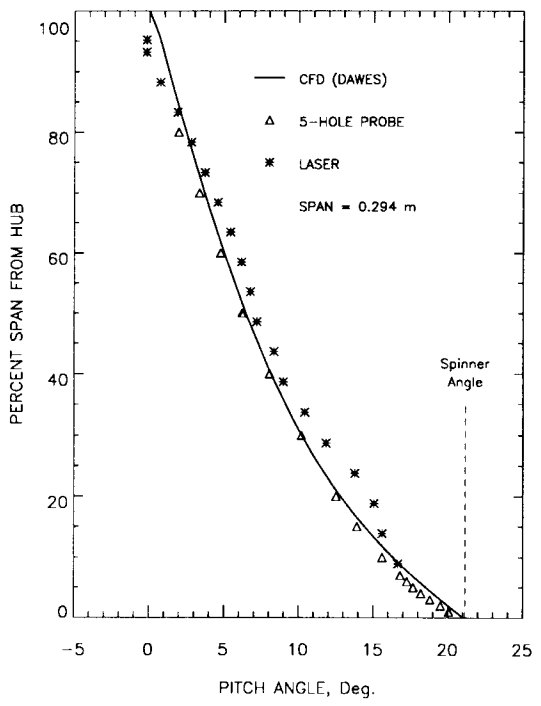

Figure 2 Measured and predicted pitch angle distribution at rotor inlet station J=23.

MEASUREMENT UNCERTAINTY

The uncertainty of the individual velocity component measurements was estimated from the least squares calculation to be on the average approximately ±1.5 m/sec throughout most of the impeller passage. Through much of the impeller passage, the throughflow velocity magnitude is on the order of 75 m/sec. Thus, the uncertainty of the measured velocity components is less than 2% of the throughflow component.

In addition to the propagation of uncertainties of the measured velocity components into the calculated velocity components, the measured velocity components are subject to the uncertainties arising from window curvature effects which distort the laser anemometer probe volume. The spanwise velocity component and flow pitch angle are most susceptible to uncertainty propagation and are therefore most sensitive to window curvature effects. Based on the results shown in Figure 2, the uncertainty in pitch angle, which directly indicates the ability to resolve the spanwise velocity component, is estimated to be less than ±2 degrees for measurement locations in the outer 70% of blade span for all measurement stations up to and including station 135. Because window curvature and blade span both decrease in the rear of the impeller, the uncertainty in the pitch angle for measurement stations 165-178 should be less than ±2 degrees over the entire blade span.

COMPUTATIONAL ANALYSIS

The computational results for the LSCC flow field were obtained using the Reynolds-averaged Navier-Stokes code developed by Dawes (1988). The code solves the equations of motion in cylindrical coordinates in integral conservation form using six-sided control volumes formed by a simple H-mesh. The basic algorithm as described by Dawes (1988) is similar to a two-step Runge-Kutta method plus residual smoothing. A combined second and fourth derivative artificial viscosity model with pressure gradient switching is used to eliminate spurious "wiggles" and to control shock capturing. The eddy viscosity is obtained using the Baldwin-Lomax (1970) mixing length model. Tip clearance is handled by gradually decreasing the thickness of the blade to zero in the tip clearance and enforcing periodicity. Since this simple treatment of the tip clearance does not solve for the details in the tip clearance gap, the actual tip clearance used in the code was reduced to 60 percent of the physical tip clearance to simulate the "vena-contracta" formed by the tip clearance jet.

The solution grid has 137 streamwise points (75 points are within the blade) with clustering around the leading edge, 71 points spanwise with 4 volumes in the tip clearance, and 41 points pitchwise. The pitchwise spacing at mid-pitch is about 5 percent of pitch and the nearest points away from the blade surfaces are at about 1 percent of pitch (however, the cell centers are 0.5 percent pitch from the surfaces). The spanwise spacing varies from a maximum of about 5 percent of span at mid-span to 0.15 percent of span for the grid nodes nearest the hub and shroud (the cell centers are about 0.07 percent away from the endwalls). The maximum streamwise spacing is about 2.5 percent of meridional chord at mid-chord.

The actual spinner geometry was modeled by fitting a small diameter cylindrical section to the spinner at a radius of 107 mm. In the calculation the spinner rotation was started at grid line 8 which is 54 percent of shroud meridional chord upstream of the blade leading edge and about 12 percent chord upstream of measurement station 23. Impeller hub rotation was stopped just downstream of the trailing edge.

Convergence was determined when the mass flow error throughout the domain was deemed acceptable and the losses through the compressor stabilized. Also, velocity components at selected points in the grid were monitored to insure that the velocity field was not changing. The maximum mass flow error was 0.56% of the inlet flow and occurred near the downstream boundary. The maximum mass flow error in the compressor blade passages was 0.38% and occurred near the trailing edge.

RESULTS AND DISCUSSION

CFD analysis has been used in a synergistic fashion with the experimental effort throughout the course of the LSCC research program and this investigation is no exception. A coarse-grid flow field prediction was first generated prior to the experiment using Dawes' 3D Navier-Stokes code (Hathaway, *et al.*, 1991) to help develop an understanding for the flow field characteristics and to aid in planning the location of laser anemometer measurements. The final CFD solution, presented herein, was used to further our understanding of flow physics phenomena such as the tip clearance flow which were not completely captured during the experimental effort.

The results presented below consist of laser anemometer measurements of the velocity field along several quasi-orthogonal planes through the impeller. Ammonia-ozalid surface flow visualization results within the impeller and hot wire anemometer results obtained in the vaneless diffuser will also be presented. The main objective of the data and computational analysis presented herein is to describe the complex flow physics within a subsonic centrifugal compressor and to demonstrate the fidelity of the three-dimensional Navier-Stokes flow field analysis.

The laser anemometer and CFD results document the development of the throughflow velocity distribution through the impeller will be presented first. Secondary velocity vector plots will then be presented in order to illustrate the migration of low-momentum fluid through the impeller blade passage. Blade-to-blade distributions of the throughflow and secondary velocity components and flow pitch angles will also be presented at a few points of interest within the impeller. Finally, pitchwise distributions of the absolute flow angle will be presented in order to illustrate the mixing of the impeller exit flow in the vaneless diffuser.

Throughflow Development

The streamwise development of the throughflow velocity will be illustrated through the use of "wire-frame" plots of the quasi-meridional velocity normalized by the rotor tip speed, V_{qm}/U_t. As described in Appendix A, the quasi-meridional velocity V_{qm} approximates the throughflow velocity component at any cross-channel station in the impeller. In order to directly compare the CFD solution to the laser data, the CFD solution was first interpolated in the streamwise direction to obtain predicted values of the velocity components V_r, V_θ, V_z at the experimental measurement planes shown in Figure 1. On each plane the CFD solution was then interpolated to the same spanwise locations as the laser data. The velocity components V_{qm}, V_s, V_p, defined in Appendix A, were then determined in the same manner for both experiment and CFD relative to the experimental measurement grid. There is therefore a one-to-one correspondence between the blade-to-blade velocity profiles in the CFD and experimental wire-frame plots. The results in each plot are shown at every 5% of span, with the results nearest the shroud located at 95% of blade span from the hub, where 100% span denotes the blade tip.

The complex nature of the flow field can lead to concern over the impact of interpolating the CFD results to the laser measurement locations. Therefore, for each measurement station presented in this paper, we compared the CFD results on the two quasi-orthogonal CFD calculation planes which lie on either side of the laser measurement plane to the CFD results which were interpolated to the measurement plane. In all cases we found that the interpolation process did not alter the predicted flow field characteristics.

Favorable agreement between CFD predictions and the laser anemometer measurements is obtained at station 85 ($m/m_s = 0.14$), as shown in Figure 3a. Both the CFD and experimental results indicate an almost linear velocity distribution across the blade passage. The results obtained at station 118 ($m/m_s = 0.47$) are shown in Figure 3b. At this station, a region of low streamwise momentum appears near the shroud at about mid-pitch. This region has been referred to as the "wake" region by previous investigators (Eckardt, 1976; Krain, 1988). The wake is evident in the experimental data at both 90 and 95% span, but is only evident in the CFD solution at 95% span. Inspection of data which is not presented here indicates that the wake first begins to develop at mid-pitch at $m/m_s = 0.40$.

The results obtained at station 135, ($m/m_s = 0.64$) are shown in Figure 3c. The broken lines indicate additional results obtained at 1% span intervals from 96% to 100% span. The momentum deficit near the shroud in both the measurements and the CFD results continues to grow in magnitude. The wake centerline also moves toward the pressure side of the passage. The measured wake occupies the outer 25% of the span. Note that the CFD solution under-predicts both the maximum velocity deficit in the wake and the spanwise extent of the wake. Also note from Figures 3a,b,c that both the measured and predicted throughflow momentum in the portion of the passage which is outside the wake is nearly constant from stations 85–135.

At station 165, ($m/m_s = 0.94$) shown in Figure 3d, the measured throughflow velocity deficit in the wake is less severe than it was at station 135. However, the minimum wake velocity at 95% span is nearly unchanged between stations 135 and 165. A detailed inspection of the blade-to-blade distributions of the throughflow velocity, plotted at individual spanwise locations, indicates that the streamwise velocity throughout the lower half of the passage and near the suction surface in the upper half of the passage has dropped significantly relative to its level at station 135. This behavior makes the wake appear less severe at station 165 than at station 135. The CFD solution indicates the wake has grown to occupy a larger spanwise extent than at station 135 and that the predicted minimum wake velocity is now comparable to the measured wake minimum velocity. Station 165 is in the region of the impeller blade passage where the pressure surface is not "covered" by the suction surface. This region begins at $m/m_s = 0.85$. The observed increase in pressure surface velocity and decrease in suction surface velocity is expected as a result of unloading of the blade. There is also a shift of the wake centerline toward mid-pitch.

The results obtained at station 170 which is at a radius ratio of 0.99 are shown in Figure 3e. The CFD results agree qualitatively with the measurements. As we move from station 165 to station 170 we also note a continued unloading of the blade as well as a

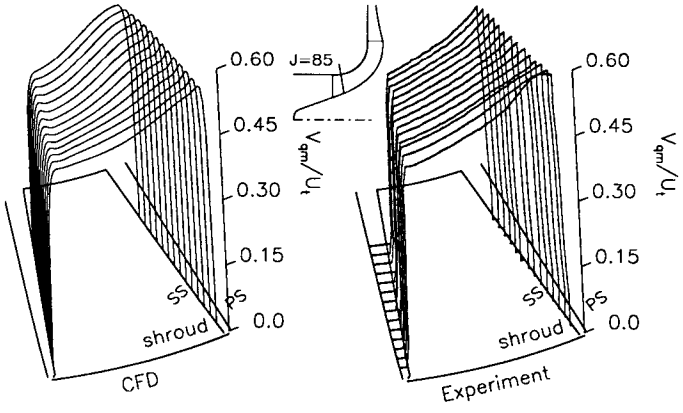

Figure 3a Distribution of quasi-meridional velocity at station 85 (m/m_s=0.149) at intervals of 5% span starting at 95% span.

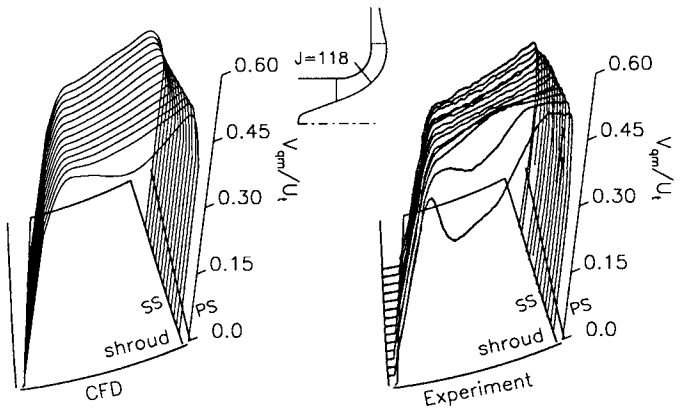

Figure 3b Distribution of quasi-meridional velocity at station 118 (m/m_s=0.475) at intervals of 5% span starting at 95% span.

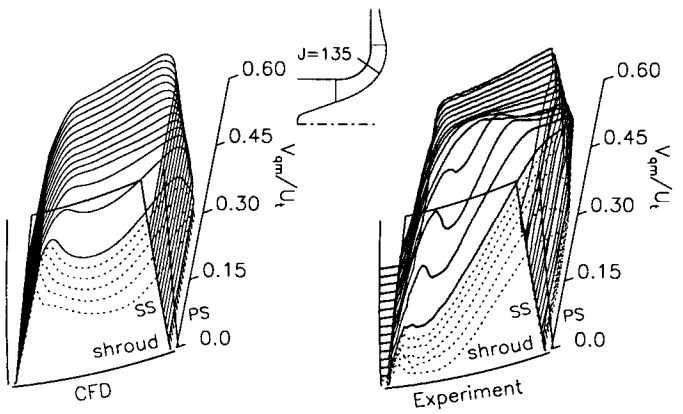

Figure 3c Distribution of quasi-meridional velocity at station 135 (m/m_s=0.644). Solid lines at intervals of 5% span starting at 95% span. Broken lines at intervals of 1% span starting at 100% span.

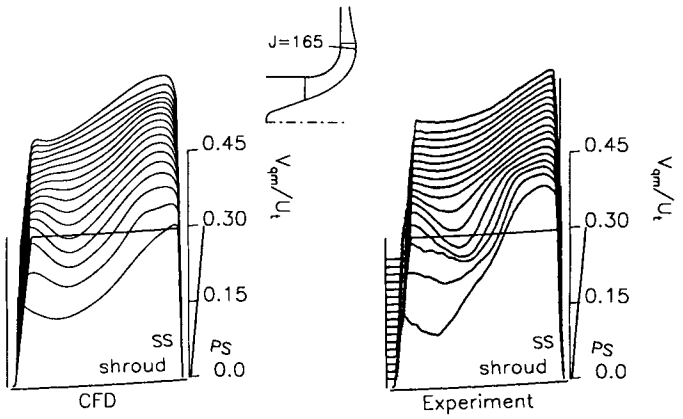

Figure 3d Distribution of quasi-meridional velocity at station 165 (m/m_s=0.941) at intervals of 5% span starting at 95% span.

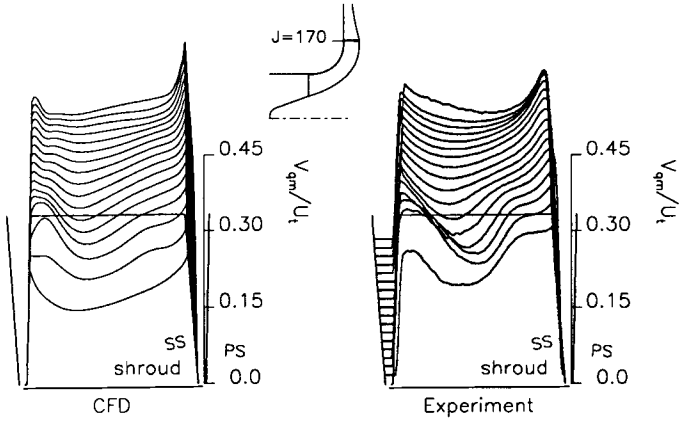

Figure 3e Distribution of quasi-meridional velocity at station 170 (m/m_s=0.990) at intervals of 5% span starting at 95% span.

continued shift of the wake centerline toward mid-pitch. The shift in wake centerline location near the exit of the impeller results from a continuing increase in the throughflow velocity near the pressure surface with increasing downstream distance. This behavior can be seen more clearly in Figure 4, where the measured blade-to-blade distributions of throughflow velocity at 90% span for stations 135–170 are plotted.

In summary, the results shown in Figure 3 indicate that the classic throughflow momentum deficit, or wake, which has been observed in centrifugal compressors by many other investigators occurs in the outer 25–35% of the span at the blade exit for this compressor. The wake is initially detected near mid-pitch, moves to the pressure surface/shroud corner of the passage, and then moves toward mid-pitch due to a continued increase in momentum in the pressure surface/shroud corner of the blade passage near the exit of the impeller.

The CFD solution predicts the location and strength of the wake near the impeller exit quite well, but under-predicts the maximum velocity deficit in the wake and the spanwise extent of the wake at

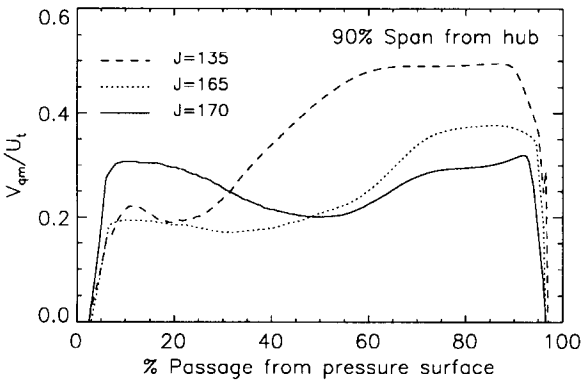

Figure 4 Blade-to-blade distribution of measured quasi-meridional velocity at 90% span for several stations near the exit of the impeller.

stations 118 and 135. These features of the CFD solution are quite sensitive to the tip clearance model used in the code. The code models the vena-contracta formed by the clearance jet crossing the sharp blade edge by using a tip clearance value which is less than the physical tip clearance. The value used in the present solution is 60% of the physical tip clearance. The effect of increasing the tip clearance used in the code from 60% to 100% of the actual clearance has been studied using a slightly coarser grid (75 streamwise points in the blade, 41 points spanwise, 41 points pitchwise). The results indicate that increasing the tip clearance in the CFD solution does indeed result in an increase in the spanwise extent of the wake and moves the wake minimum velocity closer to the pressure surface at a given station. Inspection of the impeller blade tips at the conclusion of testing indicated that the blade tip corners were not sharp. A contraction coefficient of 0.6 is therefore too small. Calculations using a larger contraction coefficient will be pursued in a future analysis of this impeller.

Secondary Velocity Development

The objective of this section is to illustrate how the secondary velocity field within the impeller contributes to the formation and movement of the throughflow wake within the impeller. The development of the secondary velocity field will be documented by presenting secondary velocity vector plots on the cross-channel measurement planes. "Secondary velocity" as used in this paper is defined as that component of the total relative velocity vector which is not aligned with streamwise CFD grid lines. A detailed definition of the spanwise and pitchwise secondary velocity components is given in Appendix A. Measured and predicted secondary velocity vectors are calculated in the same way.

As in the previous section, the CFD results were interpolated to the streamwise and spanwise location of the laser measurements. In order to provide more details of the tip clearance flow, CFD results are also shown at 98% of blade span and at 101% of blade span, which lies inside the tip clearance gap. The pitchwise location of each vector in the CFD results is fixed by the pitchwise location of the CFD grid nodes. Although the laser measurements were made at 200 points across the pitch, only the data at every third point is presented for the sake of clarity. The predicted and measured vectors are drawn to the same scale with a reference vector of length $0.5*U_t$ shown in each plot. The streamwise momentum outside of the wake region for measurement stations up to and including station 135 is on the order of $0.5*U_t$. The strength of the secondary flow relative to the throughflow can therefore be approximated by comparing the secondary velocity vector magnitudes to the reference vector magnitude in each plot.

Also shown on the predicted secondary velocity vector plots are the locations of CFD tracer particles which were released along the blade leading edge from hub to tip on either side of the leading edge stagnation line. The CFD tracer locations illustrate how low momentum fluid along the blade surface migrates toward the blade tip and becomes entrained in the tip clearance flow.

The secondary flow at station 85 near the impeller inlet is shown in Figure 5a. The CFD result shows a spanwise flow of fluid along the pressure surface in the outer 50% of the blade span. A fairly weak vortical flow is predicted at this station and the experiment is just beginning to indicate some vortical flow near the shroud. Some of the CFD tracer particles released on the suction surface at the leading edge, denoted by $*$'s, have already migrated to the tip of the blade, have been entrained in the tip clearance jet, and have begun to move toward the pressure side of the passage. Some of the CFD tracer particles released on the pressure surface at the leading edge, denoted by $\diamond$'s, have migrated to the tip of the blade, have crossed over the tip, and are also beginning to move toward the pressure side of the passage.

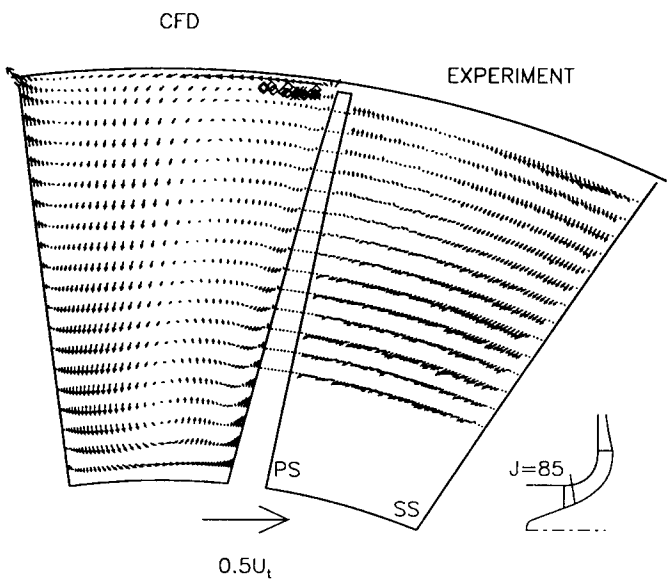

Figure 5a Secondary flow velocity vector plots at station 85 (m/m_s=0.149). Both CFD and experimental results shown at intervals of 5% span starting at 95% span with additional CFD results at 98% and 101% span. $\diamond$ and $*$ denote CFD tracers released along the blade leading edge on the pressure and suction surfaces, respectively.

At station 118, shown in Figure 5b, both the CFD and experimental results indicate that the low momentum fluid near the blade suction surface is migrating outward toward the blade tip. The CFD

solution also indicates a continuing migration of fluid toward the tip along the pressure surface. However, the experimental results indicate that the fluid moving outward along the blade pressure surface is met and turned by fluid from the vortical flow near the shroud which is moving inward toward the hub near the pressure surface/shroud corner. The vortical flow near the shroud resides in approximately the same location as the low-momentum throughflow wake region indicated in Figure 3b. The CFD and experimental results do not provide a clear indication of the origin of the inward flow which is measured in the pressure surface/shroud corner. However, the CFD tracer locations indicate that the blade leading edge particles which are now entrained within the tip clearance flow are migrating toward the pressure surface. The inward flow in the blade pressure surface/shroud corner may therefore be a result of the tip clearance flow impinging on the blade pressure surface.

The secondary flow results obtained at station 135 are shown in Figure 5c. Both the CFD and experimental results indicate a continuing migration of fluid outward toward the tip near the blade surfaces. However, the CFD results indicate that the fluid migrating outward along the blade pressure surface is now being met and turned inward by fluid moving downward near the blade pressure surface/shroud corner, just as was shown in the experimental results at station 118. In addition, the CFD tracers show further migration toward the blade pressure surface and the tracers appear to be rolling up into a vortical flow. The experimental results now show a stronger vortical flow near the shroud than indicated at station 118.

The insets in Figure 5c show additional details of the measured and predicted flows in the tip region which, for the sake of clarity, are not provided in the full-size passage view. The vector scale is different for each inset and is chosen so as to minimize overlap among vectors. Details of the predicted results in the blade pressure surface/shroud corner are shown in the left inset of Figure 5c, which is a magnified view of the full-size passage results. The results show that the inward flow in the pressure surface/shroud corner of the passage is caused by the roll-up of endwall fluid near the tip of the blade. The middle inset of Figure 5c provides further details of the measured flow field from 95–100% span at the full pitchwise resolution of the laser anemometer measurements. The results verify the roll-up of fluid predicted by the CFD solution in the pressure surface/shroud corner and show the movement of fluid near the suction surface into the tip clearance gap. Finally, the right inset provides details measured within the blade suction surface boundary layer at 85, 90, and 95% span at the full pitchwise resolution of the laser anemometer measurements. The data clearly shows the migration of the suction surface boundary layer fluid toward the shroud.

A comparison of Figure 3c and Figure 5c indicates that there is once again a strong correlation between the location of the throughflow velocity deficit and the location of strong secondary flow. As shown in Figure 3c, the magnitude of the measured normalized throughflow velocity in the pressure surface/shroud corner of the passage is V_{qm}/U_t = 0.10 — 0.15. In this region the magnitude of the secondary flow is on a par with the throughflow velocity.

At station 165, shown in Figure 5d, the CFD solution indicates a continued migration of flow outward along the blade surfaces and a well-behaved roll-up of flow in the pressure surface/shroud corner of the passage. The experimental results do not indicate outflow along the suction surface of the blade as predicted by the CFD result. We also note that a weak but discernible outward flow appears in the measurements towards the pressure-side half of the passage below about 70% span. However, the most dominant measured flow features are the strong spanwise flows in the pressure surface/shroud corner with an apparent strong reversal in spanwise flow direction (to be addressed subsequently) at about 87% span. The measurements in this region were repeated on three separate occasions and each measurement session yielded identical results.

At station 170, shown in Figure 5e, we see a dramatic change in the measured secondary flow relative to that just shown at station 165. The outward flow near the blade pressure surface, which was located below about 70% span and was quite weak at station 165, now dominates the secondary flow field in the pressure surface/shroud corner.

In order to investigate the cause of the secondary flow results shown in Figure 5d, we inspected the statistics of the individual laser anemometer measurements acquired at each of the 200 measurement points across the blade pitch. At each point a probability density distribution (p.d.d.) was constructed for all of the measurements which occurred at that point. Throughout most of the flowfield, these p.d.d.'s are Gaussian in character, which is to be expected for a turbulent flow. However, for points in the pressure surface/shroud corner at station 165, the p.d.d.'s are skewed, with long "tails" which result from the occurrence of velocities that are well below the mean velocity. The averaging method used to process all of the laser anemometer data essentially calculates the mean of each p.d.d. For Gaussian p.d.d.'s the mode, defined as the velocity which occurs most often, is close to or identical to the mean. However, for the p.d.d.'s which are skewed toward lower velocities, the mean occurs at a lower velocity than the mode.

The secondary velocity vectors shown in the inset in Figure 5d are calculated using the mode of each p.d.d. rather than the mean. The mode results yield a secondary velocity field which has no vortical structure and is more similar to that measured at station 170. Since the mode is by definition the velocity which occurs most often, the mode results are felt to be more representative of the secondary velocity field in the pressure surface/shroud corner at station 165.

The skewed p.d.d.'s in the pressure surface/shroud corner suggest that the flow is quasi-steady in this region. This might be caused by a "meandering" of the throughflow wake at station 165. The secondary velocity vectors at stations 135 and 170 were also calculated based on the mode of the p.d.d.'s. The results, which are not included here, indicate that there is no appreciable difference between the vectors calculated using the mode and those calculated using the mean. These results indicate that the flow is steady at stations 135 and 170.

The results at station 135 indicate the development of a vortex which does not appear at stations 165 and 170. The ability to "see" a vortex is highly dependent on the viewing direction used when creating the secondary velocity vectors. The fact that a vortex appears at station 135 indicates that the vortex core is well aligned with the streamwise grid lines at that station. The results shown in Figure 3 indicate that the throughflow velocity wake drifts from a location near the pressure surface toward mid-pitch as we move from station 135 to stations 165 and 170. If the vortex is associated with the wake, then the vortex core might also drift toward mid-pitch in the rear of the rotor. The vortex might therefore still be present

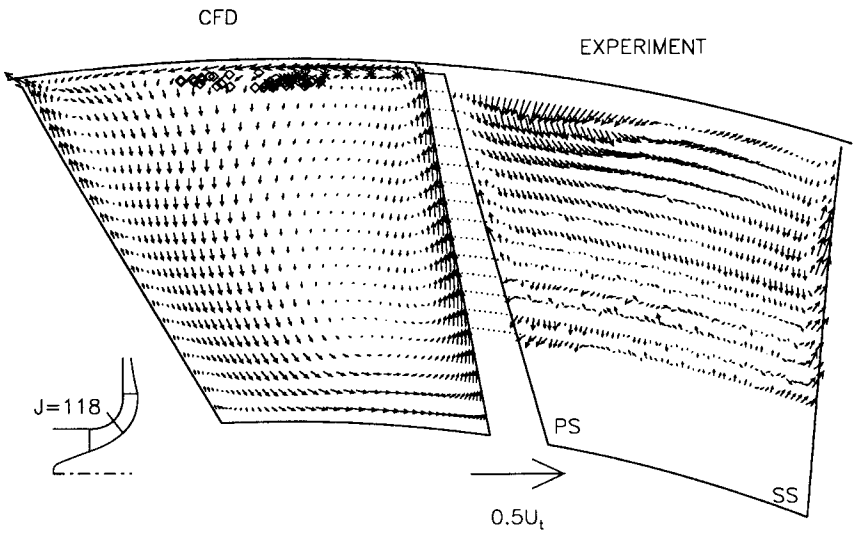

Figure 5b Secondary flow velocity vector plots at station 118 (m/m_s=0.475). Both CFD and experimental results shown at intervals of 5% span starting at 95% span with additional CFD results at 98% and 101% span. ◇ and ∗ denote CFD tracers released along the blade leading edge on the pressure and suction surfaces, respectively.

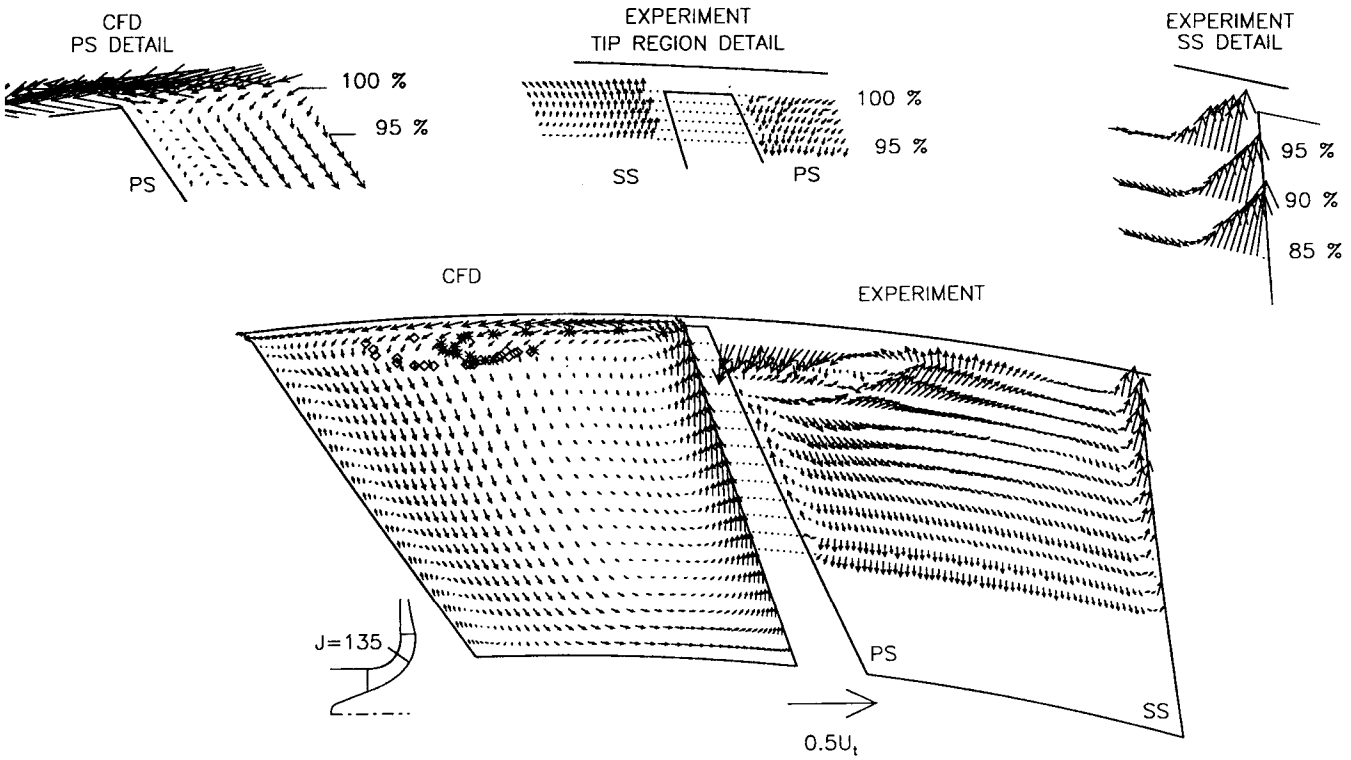

Figure 5c Secondary flow velocity vector plots at station 135 (m/m_s=0.644). Both CFD and experimental results shown at intervals of 5% span starting at 95% span with additional CFD results at 98% and 101% span. ◇ and ∗ denote CFD tracers released along the blade leading edge on the pressure and suction surfaces, respectively. Insets show additional details of the tip region flow using the actual CFD grid and full laser measurement resolution.

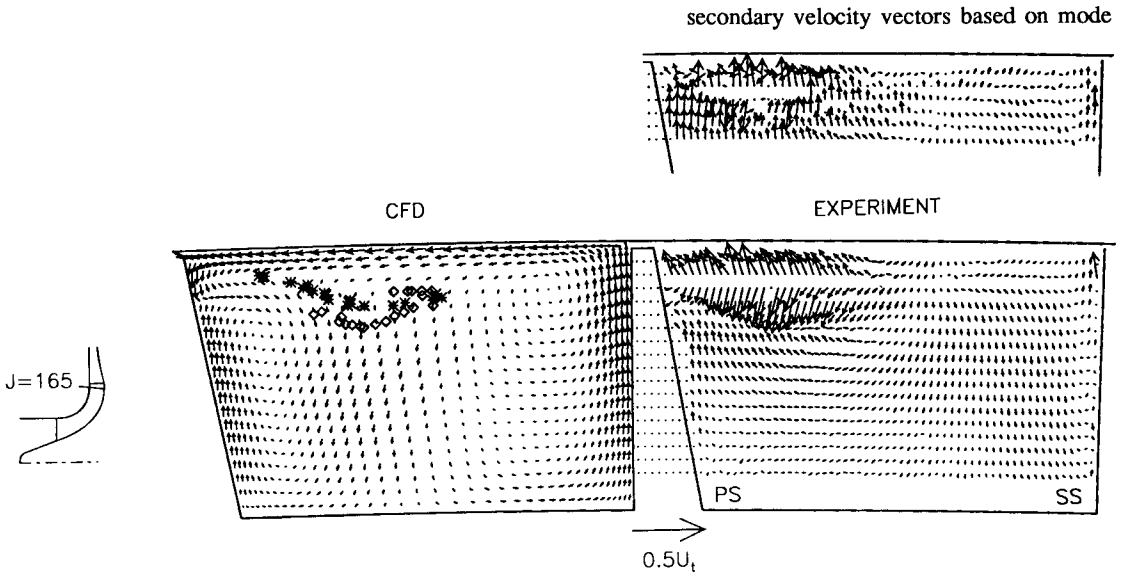

Figure 5d Secondary flow velocity vector plots at station 165 (m/m_s=0.941). Both CFD and experimental results shown at intervals of 5% span starting at 95% span with additional CFD results at 98% and 101% span. ◇ and ∗ denote CFD tracers released along the blade leading edge on the pressure and suction surfaces, respectively.

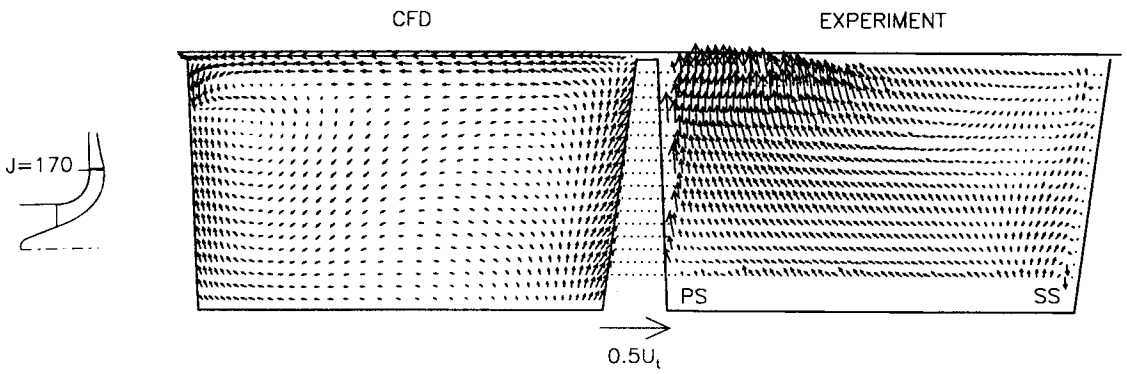

Figure 5e Secondary flow velocity vector plots at station 170 (m/m_s=0.990). Both CFD and experimental results shown at intervals of 5% span starting at 95% span with additional CFD results at 98% and 101% span. ◇ and ∗ denote CFD tracers released along the blade leading edge on the pressure and suction surfaces, respectively.

at stations 165 and 170 but is no longer evident in the secondary velocity vector plots because the core is no longer aligned with the streamwise grid lines.

The secondary velocity results and CFD particle tracers presented in Figure 5 illustrate that low momentum fluid near the blade surface migrates toward the blade tip throughout most of the impeller passage, becomes entrained in the tip clearance flow, and then migrates toward the blade pressure surface/shroud corner. A perspective view of this process is presented in Figure 6, which shows the predicted trajectories of particles which are released from hub to tip along the blade leading edge on either side of the leading edge stagnation line. The view in Figure 6 is as viewed looking upstream into the impeller blade passage from a viewpoint near the impeller exit.

The black traces in passage 1 are the trajectories of particles released on the suction surface in blade passage 1. These particles migrate up the blade surface toward the tip, are entrained in the tip clearance jet and transported across the blade passage near the shroud, and then begin to roll up in the pressure surface/shroud corner of passage 1. This roll-up can be clearly seen in Figure 6 and also in both the CFD solution and the laser measurements at station 135 (Figure 5c). The white traces in Figure 6 are the trajectories of particles released in blade passage 1 on the pressure surface outboard of 63% span. These particles migrate toward the tip, cross over the blade, move across the passage near the shroud, and roll up in the pressure surface/shroud corner in passage 2. The migration of pressure surface fluid across the tip can also be seen in the CFD solution at stations 85 and 118 (Figure 5a,b). The black traces in passage 3 in Figure 6 are the trajectories of particles released in blade passage 3 on the pressure surface inboard of 63% span. These particles begin to migrate toward the tip but are met and turned inward by the fluid which rolls up in the pressure surface/shroud corner. This behavior can also be seen in the CFD results shown in

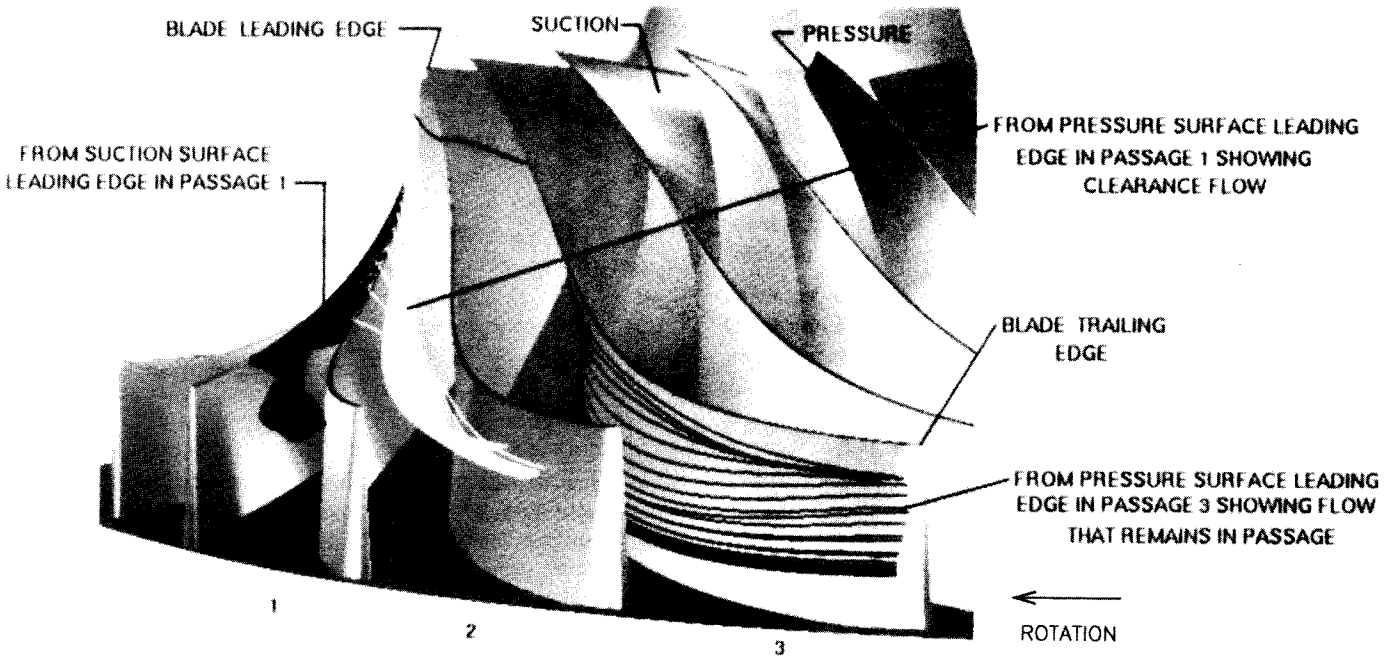

Figure 6 Perspective view of the paths of CFD tracers released on the blade surfaces near the impeller leading edge.

Figures 5c,d at stations 135 and 165. Comparison of the particle trajectories in Figure 6 with the throughflow velocity results of Figure 3 clearly demonstrates that the throughflow velocity wake is formed by the migration of low momentum fluid near the blade surfaces toward the shroud where it is entrained by the tip clearance flow and transported toward the pressure surface.

We have studied the trajectories of additional CFD tracers released all along the blade chord on the blade surfaces near the tip. These trajectories, which are not shown here, indicate that all of the fluid outboard of the tracers shown in Figure 5 originated on the blade surfaces. The tracer locations shown in Figure 5 therefore define the lower bound of the tip clearance flow.

In order to supplement the laser anemometer secondary flow measurements near the blade surfaces, the ammonia/ozalid surface flow visualization technique described by Joslyn and Dring (1986) was used to measure the flow direction along the impeller blade suction and pressure surfaces. The uncertainty in the surface flow angles measured with this technique is on the order of ±2 degrees.

The results of the ammonia/ozalid technique are shown in Figure 7. The suction surface flow traces show a significant spanwise flow toward the tip in the area between stations 85 and 135. The ammonia traces at station 85 (m/m_s = 0.14) indicate that fluid is already entering the tip clearance gap at this station. An appreciable accumulation of seed particles was observed on the shroud windows in the region m/m_s = 0.02 — 0.30, which provides further evidence that the clearance jet develops to an appreciable strength in this region.

The ammonia traces near station 118 indicate a strong outward flow along the entire suction surface. The ammonia traces along

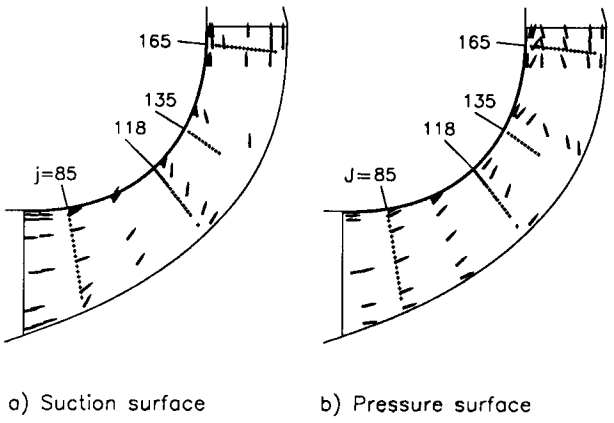

Figure 7 Meridional view of suction and pressure surface flow directions measured using ammonia/ozalid flow visualization.

the pressure surface indicate an outward flow below midspan which diminishes in strength and then becomes an inward flow as we move toward the tip. The measured velocity vector results at station 118, shown in Figure 5b, are in qualitative agreement with these ammonia/ozalid results. The ammonia traces on the pressure surface near stations 135 and 165 show several reversals from spanwise inward to spanwise outward flow in the outer half of the blade span. These changes in surface flow direction are also in qualitative agreement with the measured velocity vector results shown in Figures 5c and 5d, which indicate the presence of a strong

secondary flow in the pressure surface/shroud corner of the blade passage. The velocity vector results at station 170 (Figure 5e) do not seem to agree with the ammonia trace results on the pressure surface near the shroud. The ammonia results show that the flow near the shroud is moving inward, while the velocity vector results seem to indicate that the flow is moving outward at all spanwise locations near the pressure surface. This apparent discrepancy arises from the fact that we were not able to measure the velocity near the pressure surface at station 170 due to an optical blockage problem.

The predicted flow directions near the blade pressure surface in the rear of the impeller are shown in Figure 8, which is a meridional view of the CFD results on the first grid plane from the blade surface. A demarcation line which separates flow moving toward the hub from that moving toward the tip can be seen at about 80% span near the impeller exit. This demarcation line can also be seen in Figure 6 for the CFD tracer results near the pressure surface in passage 3. The CFD results are in excellent qualitative agreement with the pressure surface ammonia/ozalid results shown in Figure 7b at the impeller exit near the tip, which also indicate the presence of a distinct change in spanwise flow at about 80% span.

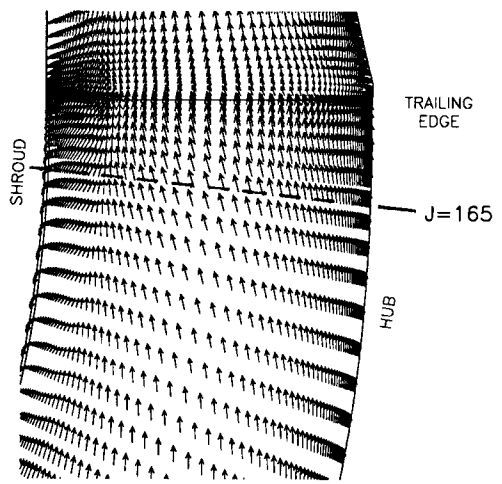

Figure 8 Meridional view of predicted velocity vectors near the pressure surface.

The secondary flow field results presented thus far have qualitatively illustrated the features of the secondary flow field and the comparison between CFD and experimental results. A more quantitative comparison between CFD and experimental results will now be provided by presenting blade-to-blade distributions of velocity and pitch angle at selected measurement locations at stations 118 and 165.

The measured and predicted distributions of the normalized quasi-meridional velocity, normalized spanwise secondary velocity, and pitch angle at 65% span at station 118 are shown in Figure 9. The comparison between predicted and measured values of V_{qm}/U_t, which approximates the throughflow velocity, are excellent. The extent of the suction and pressure surface boundary layers

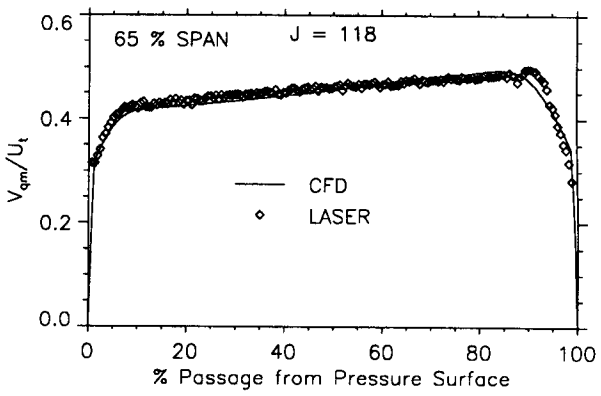

Figure 9a Blade-to-blade distribution of quasi-meridional velocity at 65% span for station 118 (m/m_s=0.475).

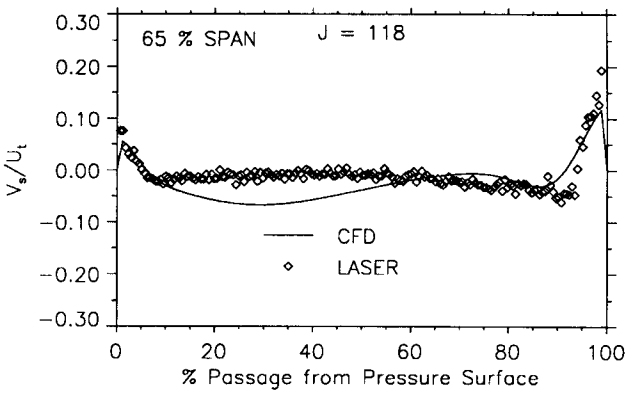

Figure 9b Blade-to-blade distribution of spanwise secondary velocity at 65% span for station 118 (m/m_s=0.475).

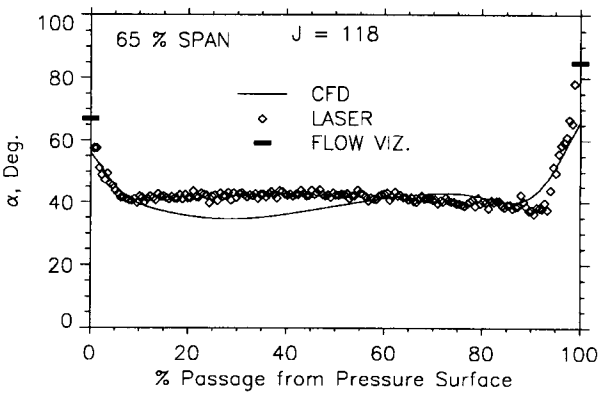

Figure 9c Blade-to-blade distribution of pitch angle at 65% span for station 118 (m/m_s=0.475).

are clearly shown. The laser anemometer measurements of the normalized spanwise secondary velocity, V_s/U_t, (see Figure 9b) indicate appreciable outflow near both the pressure and suction surfaces and a weak inflow across the remainder of the passage. Note that the outflow regions shown in Figure 9b closely correspond to the blade boundary layers shown in Figure 9a. The ability of the laser measurements to accurately resolve the spanwise velocity component is illustrated in Figure 9c where we see that the pitch angles, α, measured on the blade surfaces with the ammonia/ozalid flow visualization technique are in close agreement with the near-surface pitch angles measured with the laser anemometer.

Measured and predicted pitch angle distributions as well as the ammonia/ozalid surface flow angle results at 20, 80 and 95% span for station 165 are shown in Figure 10. At 80 and 95% span the pitch angle distributions derived from both the mean and mode of the laser measurements are shown. As discussed previously, the mode results are considered to be more representative of the flow in this region than are the mean results. The grid normal at station 165 has a pitch angle of 85 degrees. Therefore, a flow pitch angle which is greater than 85 degrees indicates a spanwise flow toward the shroud while a flow pitch angle which is less than 85 degrees indicates a spanwise flow toward the hub.

There is no appreciable spanwise flow across the entire passage at the 20% span location. The laser measurements do not indicate a large change in flow angle near the pressure surface between 80 and 95% span. However, the CFD and ammonia/ozalid results indicate a change in pitch angle on the pressure surface on the order of 50 degrees between these two spanwise locations. Note that all three techniques also indicate a relatively weak spanwise flow along the suction surface at all immersions.

Impeller Wake Mixing

Mixing phenomena downstream of centrifugal impellers are quite complex. At the impeller exit a viscous blade wake is present at all spans and a throughflow velocity wake is present near mid-pitch in the outer 30% of the blade span. In order to study wake mixing phenomena, laser anemometer measurements were acquired at four measurement stations in the vaneless diffuser at radius ratios of 1.01, 1.02, 1.04, and 1.06. The absolute flow angle distributions acquired at these stations will be used to illustrate the mixing in the LSCC vaneless space. The results provide an indication of the incidence angle variation into the diffuser vanes if a vaned diffuser were present.

The blade-to-blade variation in absolute flow angle at 50% span is shown in Figure 11a for the four measurement stations in the vaneless diffuser. The results are shown across two complete blade pitches, with the blade centered at 0% blade pitch. For each radius ratio, the flow angle variation is presented as the difference between the local flow angle, β, and the minimum flow angle at that radius ratio, β_{min}. At radius ratios of 1.01 and 1.02 the flow angle variation across the viscous blade wake is more than 30 degrees. This angle variation decreases rapidly to levels below 10 degrees at radius ratios of 1.04 and 1.06. The flow angle variation across the remainder of the blade passage is less than 6 degrees at all radius ratios.

The pitchwise variation in flow angle at 90% span is shown in Figure 11b. At this spanwise location, the flow exiting the impeller contains a throughflow velocity wake as well as a viscous

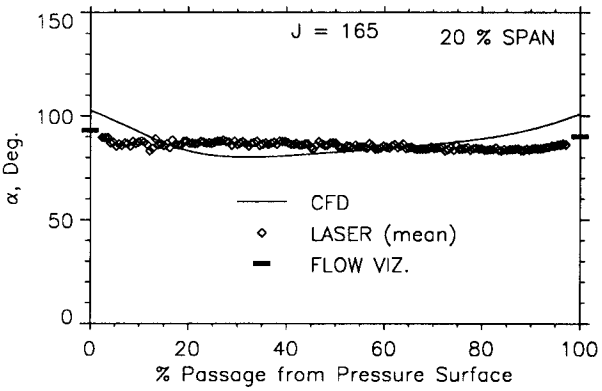

Figure 10a Blade-to-blade distribution of pitch angle at 20% span for station 165 (m/m_s=0.941).

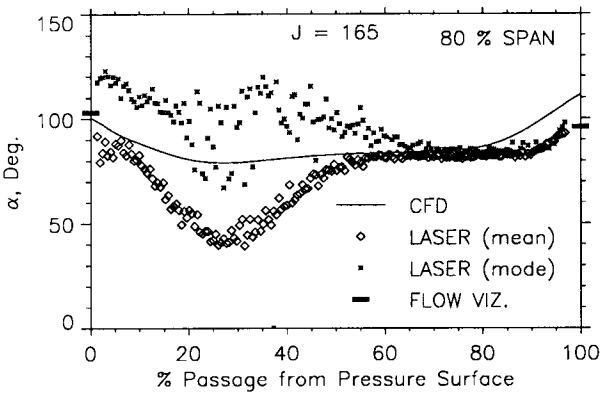

Figure 10b Blade-to-blade distribution of pitch angle at 80% span for station 165 (m/m_s=0.941).

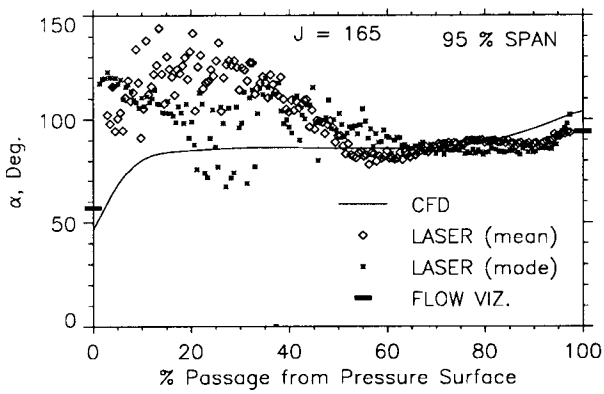

Figure 10c Blade-to-blade distribution of pitch angle at 95% span for station 165 (m/m_s=0.941).

blade wake. The blade is thinner at 90% span than at 50% span, which contributes to a weaker viscous blade wake than at 50% span. At a radius ratio of 1.01, the absolute angle variation across the viscous wake is on the order of 20 degrees, while the angle variation across the throughflow velocity wake is on the order of 10 degrees. As we move downstream, the flow angle variation across the viscous wake decreases rapidly. However, the angle variation across the throughflow wake decreases much more slowly. As a result, the variation in absolute angle across the viscous and throughflow velocity wakes is almost equal at radius ratios of 1.04 and 1.06.

Hot wire anemometer surveys of the flow field were acquired at a radius ratio of 1.06 using a slanted hot wire measurement technique described by Hanson, *et al.*, (1992). The primary purpose of this exercise was to provide an independent check on the accuracy of the laser anemometer measurement technique. The hot wire and laser anemometer results are shown in Figure 12. Both measurements indicate flow migrating towards the shroud in the viscous wake region (towards the right hand side of each plot) and in the throughflow wake region (towards the left hand side of each plot over the upper 50% immersion).

FIDELITY OF THE LOW SPEED COMPRESSOR FLOW FIELD SIMULATION

The LSCC was designed to generate a flow field which is aerodynamically similar to that found in high-speed subsonic centrifugal compressors, as described by Wood, *et al.*, (1983) and Hathaway, *et al.*, (1991). If the flow field which has been investigated in the LSCC can be shown to indeed be similar to that found in actual subsonic centrifugal compressors, then the results presented here can be used to assess the accuracy of Navier-Stokes analyses and the lessons learned can be used with confidence when analyzing actual high-speed impellers. In order to determine how well the LSCC flow field simulates that found in a high-speed subsonic compressor, the throughflow velocity in the LSCC will be compared with the throughflow velocity measured in two 4:1 pressure ratio, 30° backswept, impellers as reported by Krain and Hoffman (1989, 1990). These impellers will be denoted as Rotor I and Rotor II. Rotor II is similar to Rotor I, but features a reduction in exit blade height of approximately 30%. The tip speed of Rotor I is 470 m/sec and the

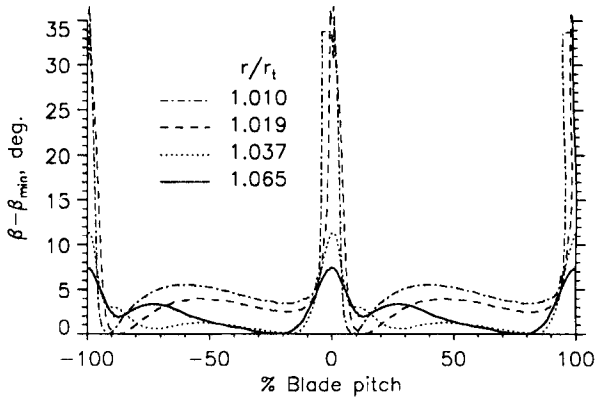

Figure 11a Pitchwise distribution of absolute flow angle difference, $\beta-\beta_{min}$, in the vaneless diffuser at 50% span.

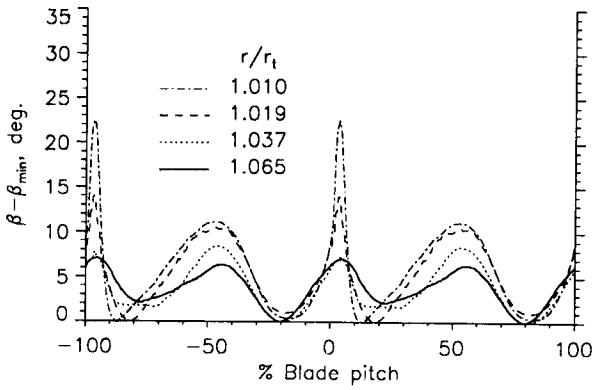

Figure 11b Pitchwise distribution of absolute flow angle difference, $\beta-\beta_{min}$, in the vaneless diffuser at 90% span.

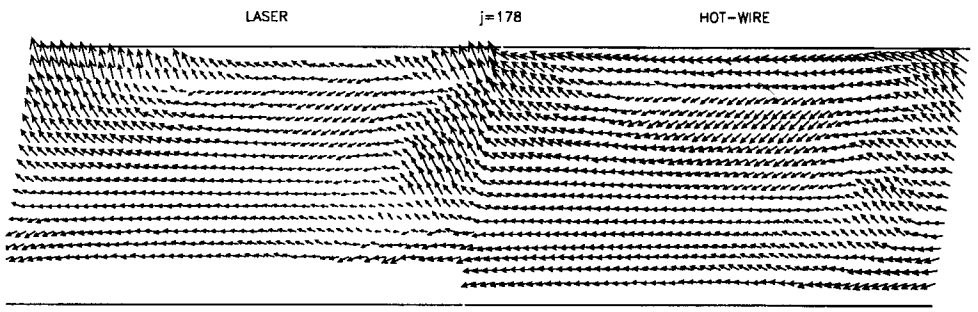

Figure 12 Comparison of laser and hot-wire anemometer measurements of secondary velocity vectors at station 178 (r/r_t=1.065).

tip clearance is 0.2 mm at the exit and 0.5 mm at the inlet. The exit blade span of the impeller is 14.7 mm, which yields a tip clearance based on exit blade span of 1.4% (0.2 mm) at the exit and 3.4% (0.5 mm) at the inlet. The tip clearance of the LSCC based on exit blade span is 1.8% (2.54 mm) and is constant from inlet to exit.

The LSCC results are shown in Figure 3 and Rotor I&II results are shown in Figure 13. Rotor I&II results are shown at 10, 30, 50, 70, and 90% span at each station, while the LSCC results presented in Figure 3 are shown every 5% of span starting at 95% span. The velocity component measured by Krain and Hoffman, denoted herein as V_{st}, is the velocity component which is tangent to the shroud in the meridional direction. The velocity component measured in the LSCC, V_{qm}, is tangent to the local streamwise grid lines, which are tangent to the shroud at 100% blade span and tangent to the hub at 0% blade span. While V_{st} and V_{qm} are not identical velocity components, they are very similar.

The throughflow velocity wake first appears in Rotor I results near the pressure surface at station III and occupies at least 10% of span at this station. This result compares favorably to that measured in the LSCC at station 118, shown in Figure 3b. The LSCC results at station 135 however do not agree with Rotor I results at station IV. The wake in the LSCC is close to the blade pressure surface at this station, while the wake in Rotor I remains near mid-pitch. The wake in Rotor I penetrates to 50% span while that in the LSCC only penetrates to 75% span, which is probably due to the fact that the tip clearance in the inlet region of Rotor I is more than double that of the LSCC. In moving from station V to VI in Rotor I, the velocity near the pressure surface rises while the velocity near the suction surface falls, indicating a reduction in blade loading. This behavior is similar to that found in the LSCC as we proceed from station 165–170.

The movement of the Rotor I wake toward mid-pitch at station IV might result from the low-momentum fluid in the wake being subjected to a larger cross-passage pressure gradient than in the LSCC. This may indeed be what is occurring if the results from rotor II (Krain & Hoffman, 1990) are considered. Since the throughflow velocity in Rotor II is somewhat higher than in Rotor I, while the cross-passage pressure gradient is similar for both rotors (the overall pressure ratio for both rotors is similar), it would seem reasonable to expect that the low-momentum wake fluid in Rotor II would remain closer to the pressure side of the passage than the wake fluid in Rotor I. The plane IV results measured in Rotor II, shown in Figure 13e, confirm that the wake is located closer to the pressure surface than it is in Rotor I. In addition, the wake in Rotor II does not penetrate below 70% span, which agrees favorably with the wake penetration to 75% span in the LSCC at station 135.

Analysis of Rotor I, Rotor II, and the LSCC with a one-dimensional centrifugal compressor performance prediction code shows that the relative velocity ratio (exit velocity/inlet tip velocity) of the LSCC falls between that of Rotor I and Rotor II.

In summary, the throughflow development in the LSCC impeller is similar to that in Krain's impellers. Differences between the LSCC throughflow characteristics and those in Rotors I&II are on the same order as the differences between the two high-speed rotors. Since the throughflow development is tightly coupled to the secondary flow development, the secondary flow field characteristics in the LSCC should indeed be similar to those which exist in high-speed subsonic centrifugal impellers.

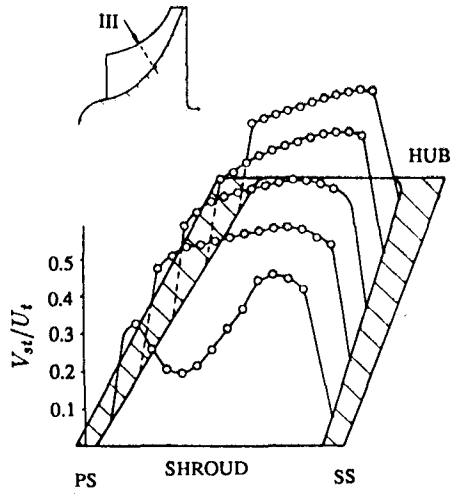

Figure 13a Rotor I, measurement plane III (m/m_s=0.4).

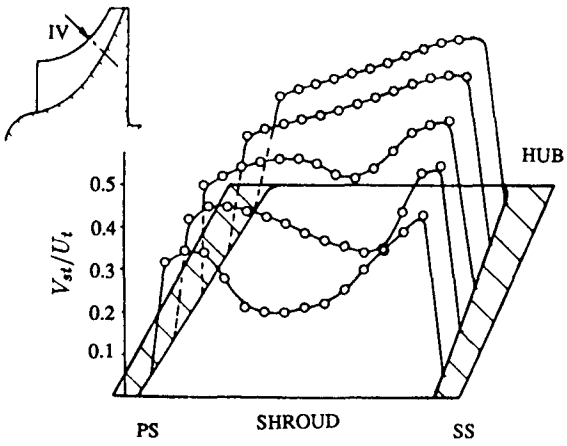

Figure 13b Rotor I, measurement plane IV (m/m_s=0.6).

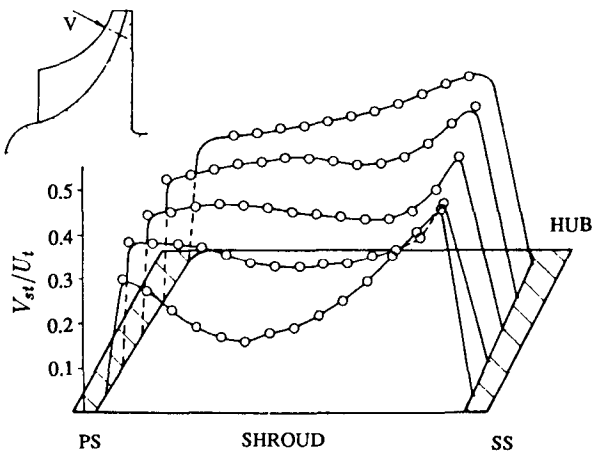

Figure 13c Rotor I, measurement plane V (m/m_s=0.8).

Figure 13 Throughflow measurements in 4:1 pressure ratio compressors by Krain and Hoffman (1989, 1990).

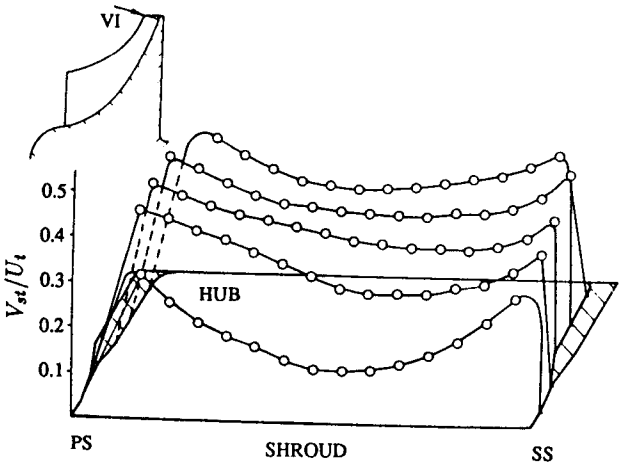

Figure 13d Rotor I, measurement plane VI (m/m_s=1.004).

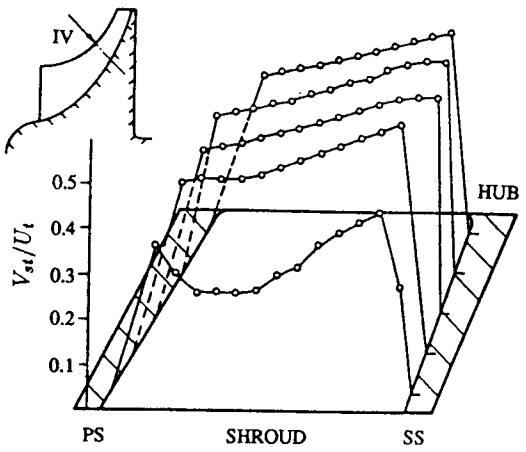

Figure 13e Rotor II, measurement plane IV (m/m_s=0.6).

SUMMARY AND CONCLUSIONS

The results presented herein represent an extensive computational and experimental effort to document the velocity field within the NASA Low Speed Centrifugal Compressor (LSCC). The large impeller passage size provides considerable optical access to the flow field and enables measurements of the three—dimensional velocity field throughout the impeller blade passage. In several cases the measurements provide details within the blade boundary layers. Independent validation of the laser measurements via 5–hole probe and hot-wire anemometer surveys as well as ammonia/ozalid surface flow visualization results provides a high degree of confidence in the laser anemometer results.

The laser anemometer measurements and the CFD solution complement one another in illustrating the flow physics within the impeller. Laser anemometer measurements confirm that the low momentum fluid near the blade surfaces migrates outward toward the tip of the blade as predicted by the CFD solution. Particle traces done on the CFD solution indicate that the fluid which moves up the blade pressure and suction surfaces is entrained into the tip clearance jet. The particle traces also show that this fluid is then transported toward the pressure side/shroud corner of the passage, where it contributes to the formation of the characteristic throughflow momentum wake which is found in unshrouded centrifugal compressor impellers.

The throughflow momentum wake region which is generated as a result of the tip clearance flow mixes out more slowly than does the viscous blade wake as the flow moves through the vaneless diffuser. The flow field in the vaneless space near the shroud surface is therefore composed of two low-momentum regions — one from the viscous blade wake and one from the throughflow momentum wake.

The development of the throughflow velocity field within the LSCC is shown to be qualitatively similar to that measured in a high speed 4:1 pressure ratio centrifugal compressor. The experimental results presented provide a representative view of the flow physics within unshrouded centrifugal compressor impellers and should be useful in assessing the ability of viscous flow codes to accurately predict the flow physics within centrifugal compressors.

ACKNOWLEDGMENTS

The authors would like to acknowledge the innumerable personnel without whose support this research endeavor would not have been possible. In particular the authors would like to thank Bill Darby, Bob Davis, John DeArmon, Marty Pietrasz, Rick Senyitko, Charles Wasserbauer, and Hal Weaver for their support of the LSCC experiment; Glenn Christman, Tim Hepner, and Mark Wernet for their support and advice relative to laser anemometer hardware and software; and Bruce Reichert, Kurt Hansen, and Andy Hiedinger for acquiring the hot-wire anemometer results.

REFERENCES

Ahmed, N. A. and Elder, R. L., 1990, "Flow Investigation in a Small High Speed Impeller Passage Using Laser Anemometry," ASME Paper No. 90-GT-233.

Baldwin, B. and Lomax, H., 1970, "Thin Layer Approximation and Algebraic Model for Separated Turbulent Flows," AIAA Paper 78-257.

Bansod, P., and Rhie, C. M., 1990, "Computation of Flow Through a Centrifugal Impeller with Tip Leakage," AIAA Paper No. 90–2021.

Dawes, W. N., 1988, "Development of a 3-D Navier Stokes Solver of Application to all Types of Turbomachinery," ASME Paper 88-GT-70.

Eckardt, D., 1976, "Detailed Flow Investigations Within a High-Speed Centrifugal Compressor Impeller," ASME Journal of Fluids Engineering, Vol. 98, pp. 390-402.

Fagan, J. R., and Fleeter, S., 1991, "Impeller Flow Field Measurement and Analysis," ASME Journal of Turbomachinery, Vol. 113, No. 4, pp. 670–179.

Farge, T. Z., Johnson, M. W., and Maksoud, T. M. A., 1989, "Tip Leakage in a Centrifugal Impeller," ASME Journal of Turbomachinery, Vol. 111, pp. 244-249.

Hah, C., and Krain, H., 1990, "Secondary Flows and Vortex Motion in a High- Efficiency Backswept Impeller at Design and Off-Design

Conditions," ASME Journal of Turbomachinery, Vol. 112, pp. 7-13.

Hanson, K. A., Heidinger, A. K., Holder, C. M., and Reichert, B. A., 1992, "A Three-Dimensional Unsteady Hot-Wire Technique for the NASA Low-Speed Centrifugal Compressor,". NASA TM-105339.

Hathaway, M. D., Wood, J.R., and Wasserbauer, C.W., 1991, "NASA Low Speed Centrifugal Compressor for 3-D Viscous Code Assessment and Fundamental Flow Physics Research," ASME Paper No. 91–GT–140.

Joslyn, H. D., and Dring, R. P., 1986, "Surface Indicator and Smoke Flow Visualization Techniques in Rotating Machinery," Heat Transfer and Fluid Flow in Rotating Machinery, Hemisphere Publishing Corp., pp. 156–169.

Krain, H., 1988, "Swirling Impeller Flow," ASME Journal of Turbomachinery, Vol. 110, pp. 122-128.

Krain, H. and Hoffman, W., 1989, "Verification of an Impeller Design by Laser Measurements and 3D-Viscous Flow Calculations," ASME Paper No. 89–GT-159.

Krain, H. and Hoffman, W., 1990, "Centrifugal Impeller Geometry and its Influence on Secondary Flows," in AGARD Secondary Flows in Turbomachines."

Moore, J. and Moore, J. G., 1990, "A prediction of 3-D Viscous Flow and Performance of the NASA Low-Speed Centrifugal Compressor," ASME Paper No. 90-GT-234.

Nichols, C. E., Jr., 1987, "Preparation of Polystyrene Microspheres for Laser Velocimetry in Wind Tunnels," NASA TM 89163.

Rohne, K. H., and Banzhaf, M., 1990, "Investigation of the Flow at the Exit of an Unshrouded Centrifugal Impeller and Comparison With the "Classical" Jet-Wake Theory," ASME Journal of Turbomachinery, Vol 113, No. 4, pp 654–659.

Senoo, Y., Yamaguchi, M., and Nishi, M., 1968, "A Photographic Study of Three-Dimensional Flow in a Radial Compressor," ASME Paper No. 68-GT-2.

Sipos, G., 1991, Secondary Flow Loss Distribution in a Radial Compressor with Untwisted Backswept Vanes," ASME Journal of Turbomachinery, Vol 113, No. 4, pp 686–695.

Strazisar, A.J., Wood J.R., Hathaway, M.D., and Suder, K.L., 1989, "Laser Anemometer Measurements in a Transonic Axial-Flow Fan Rotor," NASA TP-2879.

Wood. J. R., Adam, P. W., and Buggele, A. E., 1983, "NASA Low-Speed Centrifugal Compressor for Fundamental Research," NASA TM 83398.

Wood, J.R., Strazisar, A.J., and Hathaway, M.D., 1990, "E/C0–2 Single Transonic Fan Rotor", in AGARD-AR-275.

Appendix A DEFINITION OF VELOCITY COMPONENTS

In order to visualize secondary flow, the total relative velocity vector must be viewed along the streamwise direction. However, in a geometrically complex channel such as a centrifugal impeller blade passage, the streamwise direction can be defined in several different ways, and each definition will yield a slightly different result for the secondary flow. This problem has been pointed out by many previous authors. The purpose of the following discussion is to document the procedure used to generate the secondary flow field results presented in this paper. The same procedure is applied to both the computational and experimental results.

The secondary flows presented in this paper are defined as the departure of the local relative velocity vector from the local streamwise grid direction. The secondary velocity vector is given by $\vec{V}_T - \vec{V}_g$, where $\vec{V}_T$ is the relative velocity vector and $\vec{V}_g$ is the projection of $\vec{V}_T$ in the local streamwise grid direction, $\vec{g}(r, \theta, z)$. The spanwise and pitchwise components of the secondary velocity vector, V_s and V_p, are the projections of the secondary velocity vector in the local spanwise and pitchwise grid directions, as given by the two dot products

$$\begin{aligned} V_s &= (\vec{V}_T - \vec{V}_g) \cdot \hat{g}_s \\ V_p &= (\vec{V}_T - \vec{V}_g) \cdot \hat{g}_p \end{aligned} \tag{4}$$

where $\hat{g}_s$ and $\hat{g}_p$ are unit vectors in the local spanwise and pitchwise grid directions. When secondary flow results are presented in the form of vector plots in a quasi-orthogonal plane, V_s and V_p are used to determine the magnitude and direction of the plotted secondary velocity vectors.

The procedure described above is applied at each measurement grid node when processing experimental data and at each CFD grid node when processing CFD results. Thus a flow field with no secondary flow components will appear as a point at each grid node, indicating that the flow is following the streamwise grid direction. Since the local streamwise grid direction is parallel to the blade, hub, and shroud surfaces, the definition of secondary flow presented above also insures that the secondary velocity is zero at all solid surfaces.

The quasi-meridional velocity component, V_{qm}, is the vector projection of the meridional velocity vector, $\vec{V}_m$, in the local streamwise grid direction, $V_{qm} = \vec{V}_m \cdot \hat{g}_m$. Since a quasi-orthogonal plane is nearly normal to the streamwise grid direction in the meridional plane at any station in the impeller, V_{qm} is a close approximation to the throughflow velocity which crosses a quasi-orthogonal plane. V_{qm} is also a close approximation to the streamwise velocity component measured in laser anemometer investigations published by previous authors (Krain, 1988; Ahmed and Elder, 1990; Fagan and Fleeter, 1991). In these investigations, the streamwise velocity component was defined as the velocity component in the direction tangent to the shroud meridional direction at each measurement station.